





Turbulent Density Fluctuations and Proton Heating Rate in the Solar Wind from 9–20 R_{\odot}

K. Sasikumar Raja¹ , Prasad Subramanian¹, R. Ramesh², Angelos Vourlidis^{3,5} , and Madhusudan Ingale⁴

¹Indian Institute of Science Education and Research, Pashan, Pune—411 008, India; sasikumar@iiserpune.ac.in

²Indian Institute of Astrophysics, 2nd Block, Koramangala, Bangalore—560 034, India

³Applied Physics Laboratory, Johns Hopkins University, Laurel, Maryland, USA

⁴Plot No. 2, Near RSS office, Bamb Colony, Jammer Road, Bhusaval—425 201, India

Received 2017 September 20; revised 2017 October 16; accepted 2017 October 17; published 2017 November 27

Abstract

We obtain scatter-broadened images of the Crab Nebula at 80 MHz as it transits through the inner solar wind in 2017 and 2016 June. These images are anisotropic, with the major axis oriented perpendicular to the radially outward coronal magnetic field. Using these data, we deduce that the density modulation index ($\delta N_e/N_e$) caused by turbulent density fluctuations in the solar wind ranges from 1.9×10^{-3} to 7.7×10^{-3} between 9 and 20 R_{\odot} . We also find that the heating rate of solar wind protons at these distances ranges from 2.2×10^{-13} to 1.0×10^{-11} erg cm⁻³ s⁻¹. On two occasions, the line of sight intercepted a coronal streamer. We find that the presence of the streamer approximately doubles the thickness of the scattering screen.

Key words: occultations – scattering – solar wind – Sun: corona – Sun: radio radiation – turbulence

1. Introduction

The solar wind exhibits turbulent fluctuations in velocity, magnetic field, and density. Traditionally, researchers have attempted to understand this phenomenon within the framework of incompressible magnetohydrodynamic (MHD) turbulence (e.g., Goldstein et al. 1995). However, density fluctuations are not explained in this framework, and remain a relative enigma despite noteworthy progress (e.g., Hnat et al. 2005; Shaikh & Zank 2010; Banerjee & Galtier 2014). While most of the data used for solar wind turbulence studies are from in situ measurements made by near-Earth spacecraft, density fluctuations can often be inferred via remote sensing observations, typically at radio wavelengths. Examples include angular broadening of point-like radio sources observed through the solar wind (Machin & Smith 1952; Hewish & Wyndham 1963; Erickson 1964; Blesing & Dennison 1972; Dennison & Blesing 1972; Sastry & Subramanian 1974; Armstrong et al. 1990; Anantharamaiah et al. 1994; Ramesh et al. 1999, 2001, 2006, 2012; Kathiravan et al. 2011; Mugundhan et al. 2016; Sasikumar Raja et al. 2016), interplanetary scintillations (IPS; Hewish et al. 1964; Cohen & Gundermann 1969; Ekers & Little 1971; Rickett 1990; Manoharan et al. 2000; Bisi et al. 2009; Tokumaru et al. 2012, 2016), spacecraft beacon scintillations (Woo & Armstrong 1979), interferometer phase scintillations using Very Long Baseline Interferometers (VLBI; Cronyn 1972), spectral broadening using coherent spacecraft beacons (Woo & Armstrong 1979), and radar echoes (Harmon & Coles 1983).

A related problem is the issue of turbulent heating in the inner solar wind. It is well known that the expansion of the solar wind leads to adiabatic cooling, which is offset by some sort of heating process (Richardson et al. 1995; Matthaeus et al. 1999). The candidates for such extended heating range from resonant wave heating (Cranmer 2000; Hollweg & Isenberg 2002) to reconnection events (e.g., Cargill & Klimchuk 2004). Some studies have attempted to link

observations of density turbulence with kinetic Alfvén waves that get resonantly damped on protons, consequently heating them (Chandran et al. 2009; Ingale 2015a).

In this paper, we investigate the characteristics of turbulent density fluctuations and the associated solar wind heating rate from 9–20 R_{\odot} using the anisotropic angular broadening of radio observations of the Crab Nebula from 2017 and 2016 June 9 to 22. The Crab Nebula passes close to the Sun on these days every year. Since its radiation passes through the foreground solar wind, these observations give us an opportunity to explore the manner in which its angular extent is broadened due to scattering of turbulent density fluctuations in the solar wind. Anisotropic scatter broadening of background sources observed through the solar wind has hitherto been reported only for small elongations (≈ 2 – $6 R_{\odot}$; e.g., Anantharamaiah et al. 1994; Armstrong et al. 1990). Imaging observations of the Crab Nebula (e.g., Blesing & Dennison 1972; Dennison & Blesing 1972) offer us an opportunity to investigate this phenomenon for elongations $\gtrsim 10 R_{\odot}$. On 2016 June 17, and 2017 June 17 and 18, a coronal streamer was present along the line of sight to the Crab Nebula; this gives us an additional opportunity to study streamer characteristics. The Parker Solar Probe (Fox et al. 2016) is expected to sample the solar wind as close as 10 R_{\odot} . In situ measurements from the SWEAP instrument on board the PSP can validate our findings regarding the density turbulence level and the proton heating rate.

The rest of the paper is organized as follows. In Section 2, we describe imaging observations of the Crab Nebula made at Gauribidanur in 2017 and 2016 June. The next section (Section 3) explains the methodology for obtaining the turbulence levels from these images. This includes a brief discussion of the structure function, some discussion of the inner scale of the density fluctuations, followed by the prescription we follow in computing the density fluctuations and solar wind heating rate at the inner scale. Section 4 summarizes our main results and conclusions.

⁵ Also at IAASARS, National Observatory of Athens, GR-15236, Penteli, Greece.

Table 1
This Table Describes the Observational Quantities and the Derived Plasma Parameters in the Solar Wind

S.No	Date	R (R_{\odot}) (3)	Peak Flux Density (Jy) (4)	ρ (5)	ϵ_{N_e} (6)	Heating Rate ($\text{erg cm}^{-3} \text{s}^{-1}$) (7)
(1)	(2)					
Line of Sight to the Crab Does Not Include a Streamer						
1	2016 Jun 12	10.18	1349	1.48	2.9E-3	3.9E-12
2	2016 Jun 18	13.46	1473	1.76	5.3E-3	1.0E-11
3	2016 Jun 19	16.83	1546	1.69	7.7E-3	1.9E-11
4	2016 Jun 20	20.27	2003	1.98	1.9E-3	2.2E-13
5	2017 Jun 09	21.13	2015	1.48
6	2017 Jun 10	17.68	1732	1.57	6.2E-3	9.2E-12
7	2017 Jun 12	10.97	1386	1.50	3.4E-3	4.7E-12
8	2017 Jun 22	26.34	2015	1.40
Line of Sight to the Crab Includes a Streamer						
9	2016 Jun 17	10.20	845	2.44
10	2017 Jun 17	9.41	901	2.51
11	2017 Jun 18	12.61	800	1.65

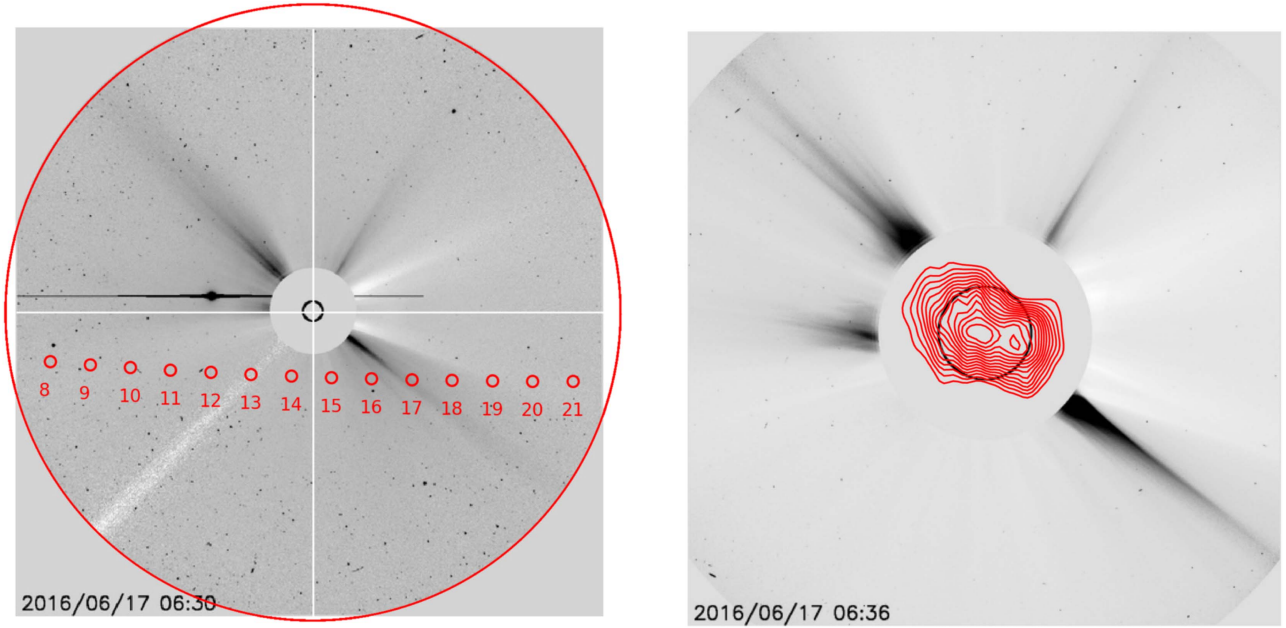


Figure 1. (Left) *SOHO*/LASCO C3 image of the solar corona (inverted grayscale image) observed on 2016 June 17 at 06:30 UT is shown. The innermost black circle indicates the solar disk (radius = $1 R_{\odot}$). The next concentric circle is the occulting disk of the coronagraph and its radius is $3.5 R_{\odot}$. The outermost circle marks a heliocentric distance of $30 R_{\odot}$. In both the images, the black features are coronal streamers. Solar north is up and east is to the left. The small circles superposed on the image represent the location of the Crab Nebula on different days during the period of 2016 June 8 to June 21. Its closest approach to the Sun is on 2016 June 14 at a heliocentric distance of $\approx 5 R_{\odot}$. The coronal streamer in the southwest quadrant occults the Crab Nebula on 2016 June 17 at a projected heliocentric distance $\approx 10.2 R_{\odot}$. The position angle (PA, measured counterclockwise from north) of the streamer is $\approx 235^{\circ}$. (Right) *SOHO*/LASCO C2 image of the solar corona (inverted grayscale) on 2016 June 17 at 06:36 UT is shown. The red contours represent observations of the solar corona using the GRAPH at 80 MHz. The elongated radio contours correspond to emission from the streamers in northeast and southwest quadrants.

2. Observations: Scatter-broadened Images of the Crab Nebula

The radio data were obtained with the Gauribidanur Radioheliograph (GRAPH; Ramesh et al. 1998; Ramesh 2011) at 80 MHz during the local meridian transit of the Crab Nebula. The GRAPH is a T-shaped interferometer array with baselines ranging from ≈ 80 to ≈ 2600 m. The angular resolution is ≈ 5 arcmin at 80 MHz, and the minimum detectable flux 5σ level) is ≈ 50 Jy for 1 s integration time and 1 MHz bandwidth. Cygnus A was used to calibrate the observations. Its

flux density is $\approx 16,296$ Jy at 80 MHz. The flux density of the Crab Nebula (when it is far from the Sun and is not therefore scatter-broadened by solar coronal turbulence) is ≈ 2015 Jy at 80 MHz. We imaged the Crab Nebula at different projected heliocentric distances shown in column (3) of Table 1 in the years 2016 and 2017.

We have used white light images of the solar corona obtained with the Large Angle and Spectrometric Coronagraph (LASCO) on board the *Solar and Heliospheric Observatory* (*SOHO*; Brueckner et al. 1995) for general context, and to identify features like coronal streamers. Figure 1 shows the

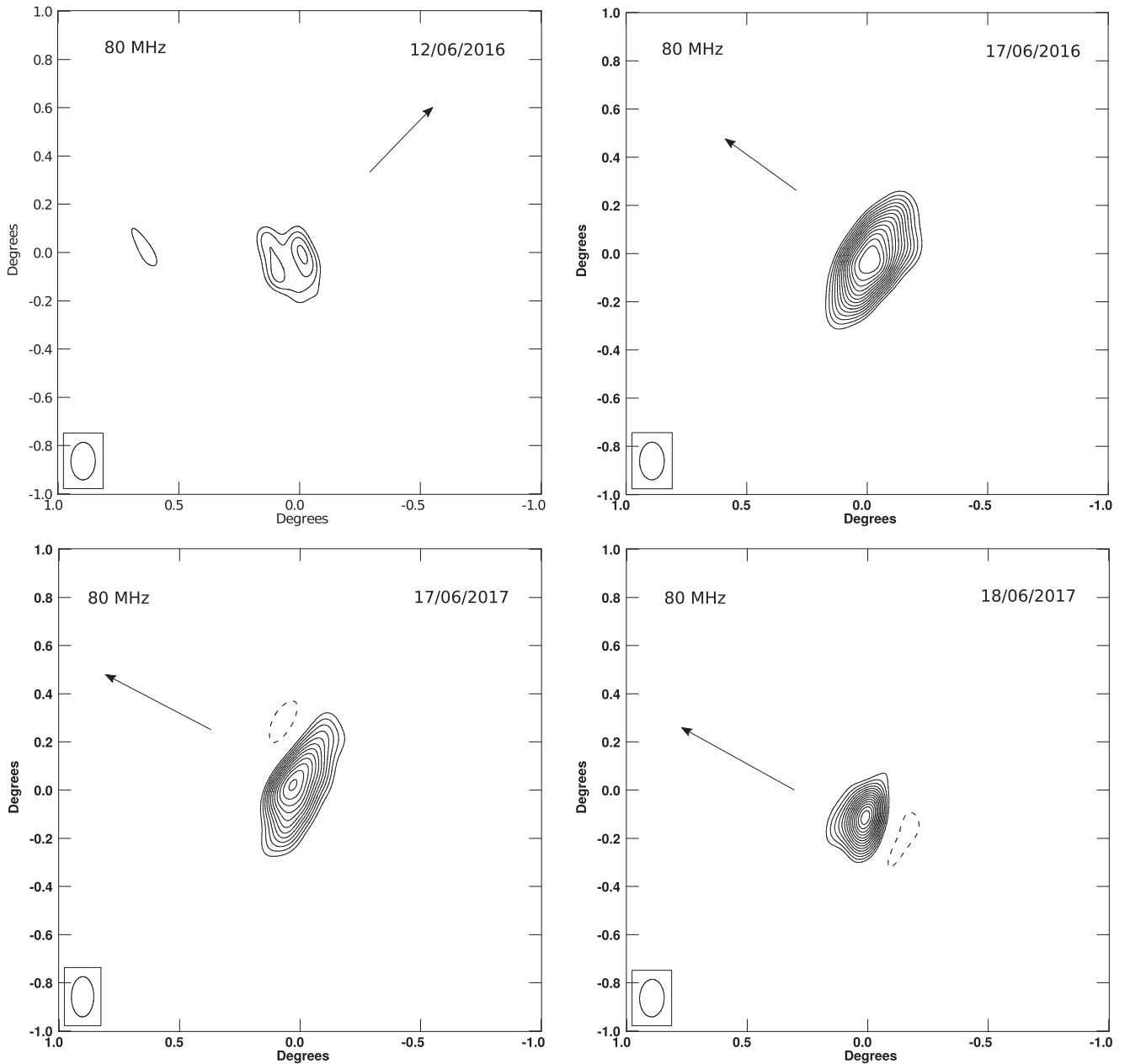


Figure 2. Image on 2016 June 12 shows the scatter-broadened Crab Nebula at a projected heliocentric distance of $10.18 R_{\odot}$ during its ingress into the inner solar wind. The images on 2016 June 17 (at $10.2 R_{\odot}$), 2017 June 17 ($9.41 R_{\odot}$), and 2017 June 18 ($12.61 R_{\odot}$) depict the scatter-broadened Crab Nebula observed through coronal streamers during its egress from the solar wind. The arrows depict the sunward direction on each day. The major axis of each image is perpendicular to the magnetic field lines, which are directed radially outward from the Sun.

white light images of the solar corona obtained with the LASCO C3 (left) and C2 (right) coronagraphs on 2016 June 17. The black features in both inverted grayscale images are coronal streamers. The location of the Crab Nebula between 2016 June 8 and 21 is marked by the red circles on the LASCO C3 images. On 2016 June 17, the Crab Nebula was observed through a streamer in the southwest quadrant. The streamer was associated with an active region NOAA 12555 located at heliographic coordinates S09W71. The contours superposed over the LASCO C2 image are from the GRAPH observations at 80 MHz showing radio emission from the streamers in northeast and southwest quadrants (Ramesh 2000).

Some representative 80 MHz GRAPH images of the Crab Nebula are shown in Figure 2. The image on 2016 June 12 was

observed through the solar wind at $10.18 R_{\odot}$ during ingress. The one on 2016 June 17 was observed at $10.20 R_{\odot}$, while the one on 2017 June 17 at $9.41 R_{\odot}$ and the one on 18 June 2017 at $12.61 R_{\odot}$ during egress. The Crab Nebula was occulted by a coronal streamer on 2016 June 17 and on 2017 June 17 and 18. These scatter-broadened images are markedly anisotropic. This aspect has been noted earlier, for the Crab Nebula (Blesing & Dennison 1972; Dennison & Blesing 1972) as well as other sources (Armstrong et al. 1990; Anantharamaiah et al. 1994). Note that the major axis of these images is always perpendicular to the heliocentric radial direction (which is typically assumed to be the magnetic field direction at these distances)—this is especially evident when the Crab is occulted by a streamer. Using the Gauribidanur Low-frequency Solar

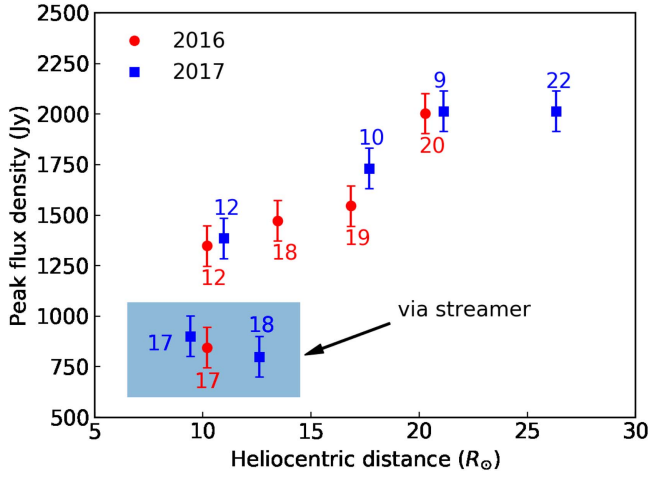


Figure 3. Peak flux density of the Crab Nebula on different days of 2016 June (red circles) and 2017 (blue squares). The red and blue data points shown in the shaded area indicate instances when the Crab Nebula was observed through a streamer in 2016 and 2017 respectively.

Spectrograph (GLOSS; Kishore et al. 2014) observations we identified that there were no transient radio bursts during the time of observations. The parameters for all observations of the Crab Nebula in 2016 and 2017 are tabulated in Table 1.

Figure 3 shows the observed peak flux density of the Crab Nebula with respect to its projected heliocentric distance. The red circles and blue squares are for the 2016 and 2017 observations respectively. Note that, in a given year, the data points obtained during ingress and egress were plotted together with the (projected) heliocentric distance.

The observations shown in the shaded region in Figure 3 represent instances where the Crab Nebula was occulted by a coronal streamer. Evidently, the peak flux density in these instances is considerably lower (as compared to the flux corresponding to a similar heliocentric distance when the Crab is not occulted by a streamer). This could be because the line of sight to the Crab Nebula passes through more coronal plasma during instances of streamer occultation, leading to enhanced scatter broadening. In turn, this leads to a larger scatter-broadened image and a consequent reduction in the peak flux density.

3. Turbulent Density Fluctuations and Solar Wind Proton Heating Rate

The angular broadening observations of the Crab Nebula described in the previous section can be used to infer the amplitude of turbulent density fluctuations and associated heating rate of protons in the solar wind. The main quantity inferred from the observations is the structure function, which is essentially the spatial Fourier transform of the visibility observed with a given baseline. The structure function is used to estimate C_N^2 , the so-called “amplitude” of the turbulent density spectrum. The density spectrum is modeled as a power law with an exponential cutoff at an “inner scale.” We assume that the inner scale is given by the proton inertial length. We elaborate on these aspects in the subsections below.

3.1. Background Electron Density and the Inner Scale

Since our aim is to estimate the level of turbulent density fluctuations in relation to the background density (N_e), we use Leblanc density model (Leblanc et al. 1998) to estimate the N_e

in the solar wind,

$$N_e(R) = 7.2 R^{-2} + 1.95 \times 10^{-3} R^{-4} + 8.1 \times 10^{-7} R^{-6} \text{ cm}^{-3}, \quad (1)$$

where “R” is the heliocentric distance in units of astronomical units (au, $1 \text{ au} = 215 R_{\odot}$). The background electron density is used to compute the inner scale of the turbulent density spectrum. We assume that the inner scale l_i is given by the proton inertial length (Verma et al. 1996; Leamon et al. 1999, 2000; Smith et al. 2001; Bruno & Trenchi 2014; Chen et al. 2014), which is related to the background electron density by

$$l_i(R) = v_A(R)/\Omega_p(R) = 2\pi/k_i(R) = 228 \times \sqrt{N_e(R)} \text{ km}, \quad (2)$$

where N_e is the electron density in cm^{-3} , k_i is the wavenumber, v_A is the Alfvén speed, and Ω_i is the proton gyrofrequency. We note that our definition differs slightly from that of Coles & Harmon (1989), Harmon (1989), and Yamauchi et al. (1998) who use $l_i = 3 \times v_A(R)/\Omega_p(R)$ and $k_i = 3/l_i$.

3.2. The Structure Function D_{ϕ}

The structure function $D_{\phi}(s)$ is defined by (Prokhorov et al. 1975; Ishimaru 1978; Coles & Harmon 1989; Armstrong et al. 1990)

$$D_{\phi}(s) = -2 \ln \Gamma(s) = -2 \ln [V(s)/V(0)], \quad (3)$$

where the quantity s represents the baseline length, $\Gamma(s)$ is the mutual coherence function, $V(s)$ denotes the visibility obtained with a baseline of length s , and $V(0)$ denotes the “zero-length” baseline visibility. The quantity $V(0)$ is the peak flux density when the Crab Nebula is situated far away from the Sun, and is unresolved; we set it to be $\approx 2015 \text{ Jy}$ at 80 MHz (Braude et al. 1970; McLean & Labrum 1985). The images of the Crab Nebula in Figure 2 are obtained by combining the visibilities from all the baselines available in the GRAPH. We are interested in the turbulent density fluctuations at the inner scale, which is the scale at which the turbulent spectrum transitions from a power law to an exponential turnover. This is typically the smallest measurable scale; we therefore compute the structure function corresponding to the longest available baseline ($s = 2.6 \text{ km}$), since that corresponds to the smallest scale.

3.3. The Amplitude of Density Turbulence Spectrum (C_N^2)

The turbulent density inhomogeneities are represented by a spatial power spectrum, comprising a power law together with an exponential turnover at the inner scale:

$$P_{\delta n}(k, R) = C_N^2(R) (\rho^2 k_x^2 + k_y^2)^{-\alpha/2} \times \exp \left[-(\rho^2 k_x^2 + k_y^2) \left(\frac{l_i(R)}{2\pi} \right)^2 \right], \quad (4)$$

where $k = \sqrt{\rho^2 k_x^2 + k_y^2}$ is the wavenumber, and k_x and k_y are the wavenumber along and perpendicular to the large-scale magnetic field respectively. The quantity ρ is a measure of the anisotropy of the turbulent eddies. In our calculations, we

use the axial ratio of the scatter-broadened images at 80 MHz (shown in Table 1) for ρ . The quantity C_N^2 is the amplitude of density turbulence, and has dimensions of $\text{cm}^{-\alpha-3}$, where α is the power-law index of the density turbulent spectrum. At large scales, the density spectrum follows the Kolmogorov scaling law with $\alpha = 11/3$. At small scales, (close to the inner scale, when $s \approx l_i$) the spectrum flattens to $\alpha = 3$ (Coles & Harmon 1989). Since we are interested in the density fluctuations near the inner scale, we use $\alpha = 3$.

Many authors use analytical expressions for the structure function that are applicable in the asymptotic limits $s \ll l_i$ or $s \gg l_i$ (Coles et al. 1987; Armstrong et al. 2000; Bastian 1994; Subramanian & Cairns 2011). However, these expressions are not valid for situations (such as the one we are dealing with in this paper) where the baseline is comparable to the inner scale; i.e., $s \approx l_i$. We therefore choose to use the General Structure Function (GSF), which is valid in the $s \ll l_i$ and $s \gg l_i$ regimes as well as when $s \approx l_i$ (Ingale et al. 2015b). In the present case, largest baseline length ≈ 2.6 km is comparable to the inner scale lengths ≈ 4.56 km. The GSF is given by the following expression:

$$D_\phi(s) = \frac{8\pi^2 r_e^2 \lambda^2 \Delta L}{\rho 2^{\alpha-2} (\alpha-2)} \Gamma\left(1 - \frac{\alpha-2}{2}\right) \frac{C_N^2(R) l_i^{\alpha-2}(R)}{(1-f_p^2(R)/f^2)} \times \left\{ {}_1F_1\left[-\frac{\alpha-2}{2}, 1, -\left(\frac{s}{l_i(R)}\right)^2\right] - 1 \right\} \text{rad}^2, \quad (5)$$

where ${}_1F_1$ is the confluent hyper-geometric function, r_e is the classical electron radius, λ is the observing wavelength, R is the heliocentric distance (in units of R_\odot), ΔL is the thickness of the scattering medium, f_p and f are the plasma and observing frequencies respectively. Substituting the model densities and $\alpha = 3$ in Equation (5) enables us to calculate C_N^2 . Following Sasikumar Raja et al. (2016), we assume the thickness of the scattering screen to be $\Delta L = (\pi/2)R_0$, where, R_0 is the impact parameter related to the projected heliocentric distance of the Crab Nebula in units of centimeters. When the Crab Nebula is occulted by a streamer, however, this estimate of ΔL is not valid. It is well known that the streamer owes its appearance to the fact that the line of sight to the streamer intercepts excess coronal plasma that is contained around the current sheet ‘‘fold.’’ It therefore stands to reason that the ΔL along a line of sight that intercepts a streamer will be larger than that along a line of sight that does not include a streamer. In view of this, we use the formula $\Delta L = (\pi/2)R_0$ and compute the density fluctuation amplitude and turbulent heating rate only for the instances where the Crab Nebula is not occulted by a streamer.

In the instances where it is occulted by a streamer, we can estimate the extra line-of-sight path length implied by the presence of the streamer. In order to do this, we first compute the structure function (Equation (5)) in the instances when the line of sight to the Crab Nebula contains a streamer. We then estimate the ratio of this quantity to the structure function (at a similar heliocentric distance) when the line of sight does not intercept, a streamer turns out to be ≈ 2 . For instance, $D_\phi(s = 2.6 \text{ km, 2016 June 17})/D_\phi(s = 2.6 \text{ km, 2016 June 12}) = 2.16$. On 2016 June 12, the Crab Nebula was situated at $10.18R_\odot$ and the line of sight to it did not pass through a

streamer. On 2016 June 17, the Crab Nebula was situated at a similar projected heliocentric distance ($10.2R_\odot$), but the line of sight to it passed through a coronal streamer. From Equation (5), it is evident that this ratio is equal to the ratio of the ΔL s in the two instances. In other words, the presence of a streamer approximately doubles the path length along the line of sight over which scattering takes place. This is nearly the same as the density enhancement in a streamer estimated from low frequency radio observations (Ramesh et al. 2000).

Although we show 80 MHz observations in this paper, we also have simultaneous observations at 53 MHz. The structure function (Equation (5)) is proportional to the square of the observing frequency (i.e., $D_\phi(s) \propto \lambda^2$). This predicts that the ratio of the structure functions at 80 and 53.3 MHz should be 0.44. Our observations yield a value of 0.43 for this ratio, and are thus consistent with the expected scaling.

3.4. Estimating the Density Modulation Index ($\epsilon_{N_e} = \delta N_{k_i}/N_e$)

The density fluctuations δN_{k_i} at the inner scale can be related to the spatial power spectrum (Equation (4)) using the following prescription (Chandran et al. 2009).

$$\delta N_{k_i}^2(R) \sim 4\pi k_i^3 P_{\delta N}(R, k_i) = 4\pi C_N^2(R) k_i^{3-\alpha} e^{-1}, \quad (6)$$

where $k_i \equiv 2\pi/l_i$. We estimate δN_{k_i} by substituting C_N^2 calculated in Section 3.3 and using $\alpha = 3$ in Equation (6). We then use this δN_{k_i} and the background electron density (N_e , Section 3.1) to estimate the density modulation index (ϵ_{N_e}) defined by

$$\epsilon_{N_e}(R) \equiv \frac{\delta N_{k_i}(R)}{N_e(R)}. \quad (7)$$

The density modulation index in the solar wind at different heliocentric distances is computed using Equation (7). The results are listed in column (6) of Table 1. The numbers in Table 1 show that the density modulation index (ϵ_{N_e}) in the solar wind ranges from 1.9×10^{-3} to 7.7×10^{-3} in the heliocentric range ≈ 10 – $20 R_\odot$. We have carried out these calculations only for the instances where the Crab Nebula is not occulted by a streamer.

3.5. Solar Wind Heating Rate

We next use our estimates of the turbulent density fluctuations (δN_{k_i}) to calculate the rate at which energy is deposited in solar wind protons, following the treatment of Ingale (2015a). The basic assumption used is that the density fluctuations at small scales are manifestations of low frequency, oblique ($k_\perp \gg k_\parallel$), Alfvén wave turbulence. The quantities k_\perp and k_\parallel refer to components of the wave vector perpendicular and parallel to the background large-scale magnetic field respectively. The turbulent Alfvén wave cascade transitions to such oblique Alfvén waves (often referred to as kinetic Alfvén waves) near the inner/dissipation scale. We envisage a situation where the turbulent Alfvén wave cascade resonantly damps on (and thereby heats) the protons at the inner scale. Since this implicitly assumes that the Alfvén waves do not couple to other modes at the inner scale, our estimate of the proton heating rate is an upper limit. As explained in Section 3.1, we assume that the inner scale is the proton inertial length, which is expressible as $l_i = v_A/\Omega_p$, where v_A is the Alfvén speed and Ω_p is the proton gyrofrequency. This way of writing the proton inertial length emphasizes its relation to the resonant damping of Alfvén waves on protons.

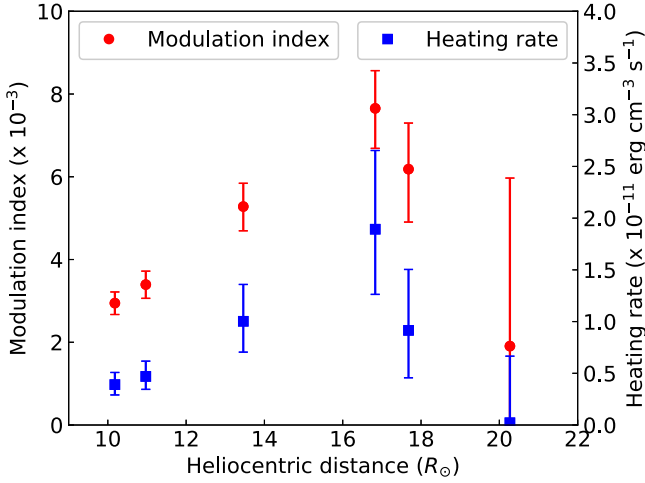


Figure 4. Variation of the density modulation index (red circles) and the solar wind proton heating rate (blue squares) with projected heliocentric distance. We note that the proton heating rate is correlated with the density modulation index.

The specific energy per unit time (ϵ , erg cm^{-3} s^{-1}) in the turbulent Alfvén wave cascade is transferred from large scales to smaller ones, until it dissipates at the inner/dissipation scale. The proton heating rate equals the turbulent energy cascade rate at the inner scale (ϵ_{k_i}), which is given by (Hollweg 1999; Chandran et al. 2009; Ingle 2015a)

$$\epsilon_{k_i}(R) = c_0 \rho_p k_i(R) \delta v_{k_i}^3(R) \text{ erg cm}^{-3} \text{ s}^{-1}, \quad (8)$$

where c_0 is a constant usually taken to be 0.25 (Howes et al. 2008; Chandran et al. 2009) and $\rho_p = m_p N_e(R)$ g cm^{-3} , with m_p representing the proton mass in grams. The quantity $k_i = 2\pi/l_i$ is the wavenumber corresponding to the inner scale (Equation (2)) and δv_{k_i} represents the magnitude of turbulent velocity fluctuations at the inner scale. The density modulation index ϵ_{N_e} and the turbulent velocity fluctuations are related via the kinetic Alfvén wave dispersion relation (Howes et al. 2008; Chandran et al. 2009; Ingle 2015a)

$$\delta v_{k_i}(R) = \left(\frac{1 + \gamma_i k_i^2(R) \rho_i^2(R)}{k_i(R) l_i(R)} \right) \epsilon_{N_e}(R, k_i) v_A(R). \quad (9)$$

The adiabatic index γ_i is taken to be 1 (Chandran et al. 2009) and the proton gyroradius (ρ_i) is given by

$$\rho_i(R) = 102 \times \mu^{1/2} T_i^{1/2} B^{-1}(R) \text{ cm}, \quad (10)$$

where μ is the ion mass expressed in terms of proton mass (≈ 1) and T_i is the proton temperature in eV. We use $T_i = 86.22$ eV, which corresponds to a temperature of 1×10^6 K.

The Alfvén speed (v_A) in the solar wind is given by

$$v_A(R) = 2.18 \times 10^{11} \mu^{-1/2} N_e^{-1/2}(R) B(R) \text{ cm s}^{-1}, \quad (11)$$

and the magnetic field strength (B) is taken to be the Parker spiral magnetic field in the ecliptic plane (Williams 1995)

$$B(R) = 3.4 \times 10^{-5} R^{-2} (1 + R^2)^{1/2} \text{ Gauss}, \quad (12)$$

where, “ R ” is the heliocentric distance in astronomical units. Equations (12), (11), (10), and (9) and the density modulation index computed in Section 3.4 are used in Equation (8) to compute the solar wind heating rate at different heliocentric

distances. These values are tabulated in column (7) of Table 1. Figure 4 depicts the density modulation index and the solar wind heating rate graphically as a function of heliocentric distance.

4. Summary and Conclusions

4.1. Summary

We have imaged (Figure 2) the Crab Nebula at 80 MHz using the GRAPH in 2017 and 2016 June, when it passed close to the Sun and was obscured by the turbulent solar wind. Since the Crab Nebula is a point source at 80 MHz when it is far from the Sun, these images are evidence of anisotropic scatter broadening of radiation emanating from it as it passes through the turbulent solar wind. We calculate the structure function with the visibilities from the longest baselines (2.6 km) used in making these images. The structure function is used to infer the amplitude of the density turbulence spectrum (C_N^2), which is then used to compute the magnitude of the turbulent density fluctuations at the inner scale (Equation (6)). This is then used to compute the density modulation index (Equation (7)). Assuming that the turbulent Alfvén wave cascade in the solar wind dissipates on protons at the inner scale, we calculate the heating rate of protons in the solar wind (Equation 8). The density modulation index and solar wind proton heating rate are plotted in Figure 4 as a function of heliocentric distance.

4.2. Conclusions

The main conclusions of this paper pertain to the anisotropy of the scatter-broadened image of the Crab Nebula, the density modulation index of the turbulent fluctuations in the solar wind and the solar wind proton heating rate from 9–20 R_{\odot} . Some of the conclusions are:

1. The 80 MHz scatter-broadened images of the Crab Nebula at heliocentric distances ranging from 9 to 20 R_{\odot} in the solar wind are anisotropic, with axial ratios typically $\lesssim 2$ (Table 1). The major axis of the Crab Nebula is typically oriented perpendicular to the magnetic field direction, as in Anantharamaiah et al. (1994) and Armstrong et al. (1990; although their observations were at much smaller distances from the Sun).
2. On 2016 June 17 and 2017 June 17, a coronal streamer was present along the line of sight to the Crab Nebula. The line of sight to the Crab encountered more coronal plasma on these days, as compared to the days when a streamer was not present. The axial ratio of the scatter-broadened images on these days was somewhat larger (≈ 2 , see Table 1) and the peak flux density is considerably lower (Figure 3), reflecting this fact. In the presence of a streamer, the path length over which scattering takes place was found to be approximately twice that of when the streamer was not present.
3. The density modulation index ($\epsilon_{N_e} \equiv \delta N_e / N_e$) at the inner scale of the turbulent spectrum in the solar wind from 9–20 R_{\odot} ranges from 1.9×10^{-3} to 7.7×10^{-3} (see Table 1). Earlier estimates of ϵ_{N_e} include Mugundhan et al. (2017) who reported 0.006 ± 0.002 from 1.6–2.2 R_{\odot} , Sasikumar Raja et al. (2016) who reported $0.001 \lesssim \epsilon_{N_e} \lesssim 0.1$ from 10–45 R_{\odot} , $0.001 \lesssim \epsilon_{N_e} \lesssim 0.02$ reported by Bisoi et al. (2014) in the distance range of 56–185 R_{\odot} , and $0.03 \lesssim \epsilon_{N_e} \lesssim 0.08$ reported by Spangler & Spitler

(2004) at 1 au ($215 R_{\odot}$). The red circles in Figure 4 depict the modulation index as a function of heliocentric distance. Figure 4 shows that the modulation index in the heliocentric distance 12–18 R_{\odot} is relatively higher. As explained in Sasikumar Raja et al. (2016), this might be because the line of sight to the Crab Nebula at these distances passes through the fast solar wind, which has relatively higher proton temperatures (Lopez & Freeman 1986). Furthermore, the density modulation index is correlated with the proton temperature (Celnikier et al. 1987). Taken together, this implies that one could expect higher values for the density modulation index in the fast solar wind.

- We interpret the turbulent density fluctuations as manifestations of kinetic Alfvén wave turbulence at small scales. Assuming that the turbulent Alfvén wave cascade damps resonantly on the protons at the inner scale, we use our estimates of the density modulation index to calculate the proton heating rate in the solar wind. We find that the estimated proton heating rate in the solar wind from 9–20 R_{\odot} ranges from 2.2×10^{-13} to 1.0×10^{-11} erg cm $^{-3}$ s $^{-1}$ (blue squares in Figure 4).

K.S.R. acknowledges the financial support from the Science & Engineering Research Board (SERB), Department of Science & Technology, India (PDF/2015/000393). P.S. acknowledges support from the ISRO RESPOND program. A.V. is supported by NRL grant N00173-16-1-G029. We thank the staff of the Gauribidanur observatory for their help with the observations and maintenance of the antenna and receiver systems there. K.S.R. acknowledges C. Kathiravan for valuable discussions related to the GRAPH observations. *SOHO*/LASCO data used here are produced by a consortium of the Naval Research Laboratory (USA), Max-Planck-Institut fuer Aeronomie (Germany), Laboratoire d’Astronomie (France), and the University of Birmingham (UK). *SOHO* is a project of international cooperation between ESA and NASA. The authors would like to thank the anonymous referee for valuable and constructive suggestions.

ORCID iDs

K. Sasikumar Raja  <https://orcid.org/0000-0002-1192-1804>
 Angelos Vourlidas  <https://orcid.org/0000-0002-8164-5948>

References

- Anantharamaiah, K. R., Gothoskar, P., & Cornwell, T. J. 1994, *JApA*, **15**, 387
 Armstrong, J. W., Coles, W. A., & Rickett, B. J. 2000, *JGR*, **105**, 5149
 Armstrong, J. W., Coles, W. A., Rickett, B. J., & Kojima, M. 1990, *ApJ*, **358**, 685
 Banerjee, S., & Galtier, S. 2014, *JFM*, **742**, 230
 Bastian, T. S. 1994, *ApJ*, **426**, 774
 Bisi, M. M., Jackson, B. V., Buffington, A., et al. 2009, *SoPh*, **256**, 201
 Bisoi, S. K., Janardhan, P., Ingale, M., et al. 2014, *ApJ*, **795**, 69
 Blesing, R. G., & Dennison, P. A. 1972, *PASAu*, **2**, 84
 Braude, S. Y., Megn, A. V., Ryabov, B. P., & Zhouck, I. N. 1970, *Ap&SS*, **8**, 275
 Brueckner, G. E., Howard, R. A., Koomen, M. J., et al. 1995, *SoPh*, **162**, 357
 Bruno, R., & Trenchi, L. 2014, *ApJL*, **787**, L24
 Cargill, P. J., & Klimchuk, J. A. 2004, *ApJ*, **605**, 911
 Celnikier, L. M., Muschietti, L., & Goldman, M. V. 1987, *A&A*, **181**, 138
 Chandran, B. D. G., Quataert, E., Howes, G. G., Xia, Q., & Pongkitwanichakul, P. 2009, *ApJ*, **707**, 1668
 Chen, C. H. K., Leung, L., Boldyrev, S., Maruca, B. A., & Bale, S. D. 2014, *GeoRL*, **41**, 8081
 Cohen, M. H., & Gundermann, E. J. 1969, *ApJ*, **155**, 645
 Coles, W. A., & Harmon, J. K. 1989, *ApJ*, **337**, 1023
 Coles, W. A., Rickett, B. J., Codona, J. L., & Frehlich, R. G. 1987, *ApJ*, **315**, 666
 Cranmer, S. R. 2000, *ApJ*, **532**, 1197
 Cronyn, W. M. 1972, *ApJ*, **174**, 181
 Dennison, P. A., & Blesing, R. G. 1972, *PASAu*, **2**, 86
 Ekers, R. D., & Little, L. T. 1971, *A&A*, **10**, 310
 Erickson, W. C. 1964, *ApJ*, **139**, 1290
 Fox, N. J., Velli, M. C., Bale, S. D., et al. 2016, *SSRv*, **204**, 7
 Goldstein, M. L., Roberts, D. A., & Matthaeus, W. H. 1995, *ARA&A*, **33**, 283
 Harmon, J. K. 1989, *JGR*, **94**, 15399
 Harmon, J. K., & Coles, W. A. 1983, *ApJ*, **270**, 748
 Hewish, A., Scott, P. F., & Wills, D. 1964, *Natur*, **203**, 1214
 Hewish, A., & Wyndham, J. D. 1963, *MNRAS*, **126**, 469
 Hnat, B., Chapman, S. C., & Rowlands, G. 2005, *PhRvL*, **94**, 204502
 Hollweg, J. V. 1999, *JGR*, **104**, 14811
 Hollweg, J. V., & Isenberg, P. A. 2002, *JGRA*, **107**, 1147
 Howes, G. G., Cowley, S. C., Dorland, W., et al. 2008, *JGRA*, **113**, A05103
 Ingale, M. 2015a, arXiv:1509.07652
 Ingale, M., Subramanian, P., & Cairns, I. 2015b, *MNRAS*, **447**, 3486
 Ishimaru, A. 1978, *Wave Propagation and Scattering in Random Media*, Vol. 1 (New York: Academic)
 Kathiravan, C., Ramesh, R., Barve, I. V., & Rajalingam, M. 2011, *ApJ*, **730**, 91
 Kishore, P., Kathiravan, C., Ramesh, R., Rajalingam, M., & Barve, I. V. 2014, *SoPh*, **289**, 3995
 Leamon, R. J., Matthaeus, W. H., Smith, C. W., et al. 2000, *ApJ*, **537**, 1054
 Leamon, R. J., Smith, C. W., Ness, N. F., & Wong, H. K. 1999, *JGR*, **104**, 22331
 Leblanc, Y., Dulk, G. A., & Bougeret, J.-L. 1998, *SoPh*, **183**, 165
 Lopez, R. E., & Freeman, J. W. 1986, *JGR*, **91**, 1701
 Machin, K. E., & Smith, F. G. 1952, *Natur*, **170**, 319
 Manoharan, P. K., Kojima, M., Gopalswamy, N., Kondo, T., & Smith, Z. 2000, *ApJ*, **530**, 1061
 Matthaeus, W. H., Zank, G. P., Smith, C. W., & Oughton, S. 1999, *PhRvL*, **82**, 3444
 McLean, D. J., & Labrum, N. R. 1985, *Solar Radiophysics: Studies of Emission from the Sun at metre Wavelengths* (Cambridge: Cambridge Univ. Press)
 Mugundhan, V., Hariharan, K., & Ramesh, R. 2017, *SoPh*, **292**, 155
 Mugundhan, V., Ramesh, R., Barve, I. V., et al. 2016, *ApJ*, **831**, 154
 Prokhorov, A. M., Bunkin, F. V., Gochelashvili, K. S., & Shishov, V. I. 1975, *Proc. IEEE*, **63**, 790
 Ramesh, R. 2000, *JApA*, **21**, 237
 Ramesh, R. 2011, in *Proc. Astron. Soc. India Conf. Ser. 2, 1st Asia-Pacific Solar Physics Meeting*, ed. A. R. Choudhuri & D. Banerjee (Bangalore: ASI), 55
 Ramesh, R., Kathiravan, C., Barve, I. V., & Rajalingam, M. 2012, *ApJ*, **744**, 165
 Ramesh, R., Kathiravan, C., & Sastry, C. V. 2001, *ApJ*, **548**, L229
 Ramesh, R., Nataraj, H. S., Kathiravan, C., & Sastry, C. V. 2006, *ApJ*, **648**, 707
 Ramesh, R., Subramanian, K. R., & Sastry, C. V. 1999, *SoPh*, **185**, 77
 Ramesh, R., Subramanian, K. R., SundaraRajan, M. S., & Sastry, C. V. 1998, *SoPh*, **181**, 439
 Ramesh, R., Subramanian, K. R., & Sastry, C. V. 2000, *ApL&C*, **40**, 93
 Richardson, J. D., Paularena, K. I., Lazarus, A. J., & Belcher, J. W. 1995, *GeoRL*, **22**, 325
 Rickett, B. J. 1990, *ARA&A*, **28**, 561
 Sasikumar Raja, K., Ingale, M., Ramesh, R., et al. 2016, *JGRA*, **121**, 11605
 Sastry, C. V., & Subramanian, K. R. 1974, *IJRSP*, **3**, 196
 Shaikh, D., & Zank, G. P. 2010, *MNRAS*, **402**, 362
 Smith, C. W., Mullan, D. J., Ness, N. F., Skoug, R. M., & Steinberg, J. 2001, *JGR*, **106**, 18625
 Spangler, S. R., & Spitler, L. G. 2004, *PhPI*, **11**, 1969
 Subramanian, P., & Cairns, I. 2011, *JGRA*, **116**, A03104
 Tokumaru, M., Fujiki, K., Kojima, M., et al. 2016, in *AIP Conf. Proc. 1720, SOLAR WIND 14: Proceedings of the Fourteenth International Solar Wind Conference*, ed. L. Wang et al. (Melville, NY: AIP), 030004
 Tokumaru, M., Kojima, M., & Fujiki, K. 2012, *JGRA*, **117**, A06108
 Verma, M. K., Roberts, D. A., Goldstein, M. L., Ghosh, S., & Stribling, W. T. 1996, *JGR*, **101**, 21619
 Williams, L. L. 1995, *ApJ*, **453**, 953
 Woo, R., & Armstrong, J. W. 1979, *JGR*, **84**, 7288
 Yamauchi, Y., Tokumaru, M., Kojima, M., Manoharan, P. K., & Esser, R. 1998, *JGR*, **103**, 6571